Hard-axis magnetization behavior and the surface spin-flop transition in antiferromagnetic Fe/Cr(100) superlattices

J. Meersschaut,[1,2,*] C. L'abbé,[1] F. M. Almeida,[1] J. S. Jiang,[2] J. Pearson,[2] U. Welp,[2] M. Gierlings,[3] H. Maletta,[3] and S. D. Bader[2]

[1]*Instituut voor Kern- en Stralingsfysica and INPAC, K.U.Leuven, Celestijnenlaan 200D, B-3001 Leuven, Belgium*
[2]*Materials Science Division, Argonne National Laboratory, Argonne, Illinois 60439, USA*
[3]*Hahn-Meitner Institut, Glienicker Strasse 100, 14109 Berlin, Germany*
(Received 12 December 2005; published 25 April 2006)

We investigated the hard-axis magnetization behavior of a biaxial antiferromagnetic Fe/Cr(100) superlattice. We discovered a surface spin-flop transition that separates the field-induced nonsymmetric state at low fields and the symmetric twisted state at higher fields. We studied the transition via realistic model calculations using the Landau-Lifshitz equations of motion, via stray field observations using magneto-optic indicator film imaging, and via polarized-neutron reflectivity measurements.

I. INTRODUCTION

Anisotropic antiferromagnetic materials are known to exhibit phase transitions that can be induced by a magnetic field. Uniaxial antiferromagnets have a transition to the bulk spin-flop phase when magnetized in the easy direction. This occurs above a critical field, where the two sublattices orient nearly ±90° with respect to the field. Apart from the behavior of the bulk, uniaxial antiferromagnetic materials may also exhibit surface phase transitions. The spins near the surface rotate into a flopped state at a field substantially smaller than the bulk spin-flop field.[1] With increasing field, the flopped state penetrates and spreads over the whole antiferromagnet.[2] Besides the theoretical work, the surface spin-flop transition was also identified experimentally in artificial antiferromagnetically coupled superlattices.[3] Ever since, this surface effect has been the subject of intense research.[4–6] Apart from the fundamental interest, the understanding of the magnetization behavior of an antiferromagnetic material near its surface may also be prerequisite for a detailed explanation of the exchange bias effect in ferromagnetic/antiferromagnetic heterostructures.[7,8]

The surface spin-flop transition is only known to occur in antiferromagnets with uniaxial anisotropy when the field is applied in the easy direction. Our contribution is to identify that the surface spin-flop transition may also occur in antiferromagnetic materials with cubic anisotropy when magnetic fields are applied along the hard axis. As a model system, we study an antiferromagnetically coupled Fe/Cr(100) superlattice. The surface spin-flop transition is illustrated with realistic calculations, based on parameters that well describe the magnetization behavior of the sample. The magnetization behavior is further investigated experimentally by means of microscopic stray field observations and via polarized-neutron reflectivity measurements.

The [Fe(4 nm)/Cr(1.1 nm)]$_{22}$ superlattice was epitaxially grown on a MgO(100)/Cr(11.1 nm) substrate/buffer via dc magnetron sputtering (base pressure 2.67×10^{-6} Pa). It was capped with a 3.9-nm-thick Cr layer to prevent oxidation. We used an Ar sputtering gas pressure of 0.2 Pa and a target

power of 100 W. The buffer and multilayer were grown at 673 K and 383 K, respectively. From x-ray and neutron reflectivity data, the refined thickness of the Fe and Cr layers was 3.6(1) nm and 1.1(1) nm, respectively, and the structural roughness was 0.6 nm.

Strong antiferromagnetic coupling between the Fe layers in the Fe/Cr multilayer is expected.[9,10] The magnetization curves, measured at room temperature with alternating gradient magnetometry, are shown in Fig. 1. We can interpret the curves as follows.[11] If the magnetic field, applied along the in-plane [010] easy axis [Fig. 1(a)], is relaxed to small values, the moments are oriented transverse to the field.[9]
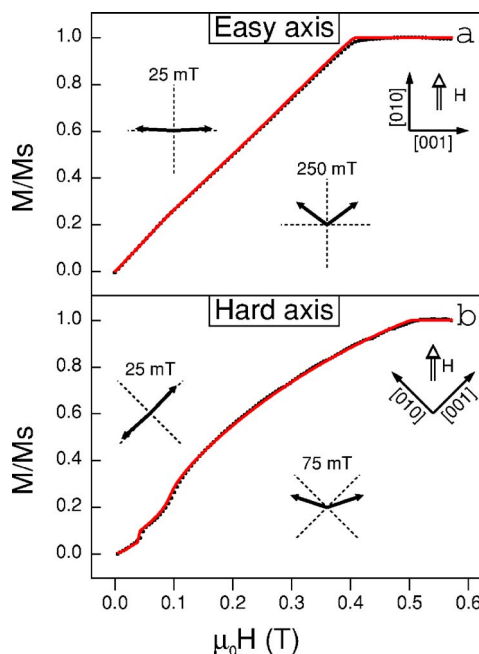

FIG. 1. (Color online) Increasing field magnetization curve for the [Fe/Cr]$_{22}$ multilayer along the easy axis (a) and hard axis (b). The red curves are fits as described in the text. The insets show the calculated spin configuration for the central iron layers 11 and 12 with respect to H and the crystalline axes (dashed lines).
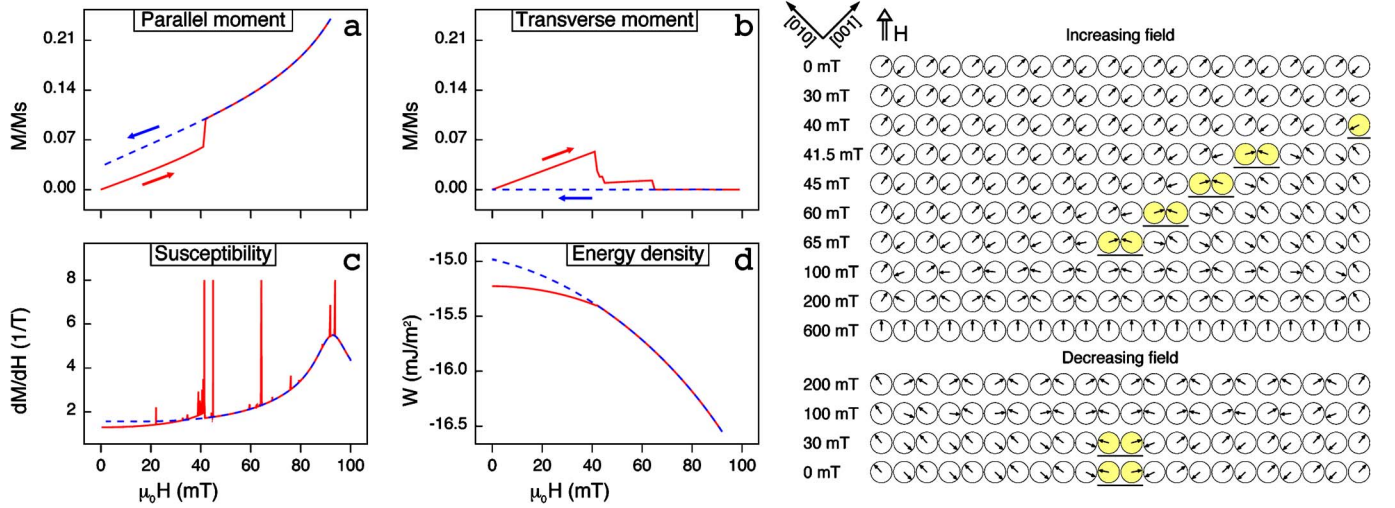
FIG. 2. (Color online) Calculated magnetization behavior as a function of external field applied along the in-plane hard axis. Left: projected moment along the field (a) and perpendicular to it (b), the static parallel susceptibility (c), and the total energy density (d). The sharp peaks in the susceptibility (c) have been cut off at the numerical value 8 for clarity. The solid red lines were calculated with increasing field, whereas the dashed blue lines were obtained on reducing the field from saturation. Right: configuration of the magnetization at selected external field values. The arrows represent the unit magnetization in each Fe layer.

With increasing field, the moments cant symmetrically towards the applied field [see the insets in Fig. 1(a)], closing to saturation at 420 mT. Figure 1(b) shows the magnetization curve for increasing fields applied along the in-plane [011] hard axis. Starting from the simple antiferromagnetic ground state at zero field, the slope at low fields corresponds to small distortions of the antiferromagnetic alignment. The distortion gives rise to a nonsymmetric configuration with a transverse component in the magnetization (see the inset for $\mu_0 H$ $=25$ mT). Above a critical field, a transition occurs from the nonsymmetric nearly antiferromagnetic state to the symmetric state (see the inset for $\mu_0 H = 75$ mT).

II. LANDAU-LIFSHITZ CALCULATIONS

The red curves in Fig. 1 are solutions of the Landau-Lifshitz equation of motion for the one-dimensional classical spin chain[4]:

$$\frac{\partial \vec{M}_i}{\partial t} = \vec{M}_i \times \vec{F}_i - \gamma[\vec{M}_i \times (\vec{M}_i \times \vec{F}_i)]. \quad (1)$$

In this equation, γ is a very small dimensionless dissipation constant, $\vec{M}_i$ is the unit magnetization of the ith layer, and $\vec{F}_i$ is the effective field related to the energy density W via $\vec{F}_i$ $=-\partial W / \partial \vec{M}_i$. The energy density is the sum of several contributions. The Zeeman term is described by W_{Zee} $=-\Sigma_{i=1}^{22}(\vec{M}_i \cdot \vec{H}) t m$. We used the layer thickness $t=3.6$ nm and the magnetization per volume $m=1.95 \times 10^6$ J/(T m^3). The magnetostatic contribution is approximated as a uniaxial anisotropy: $W_{uni} = \frac{1}{2}\Sigma_{i=1}^{22}K_d t M_{iz}^2$, with $K_d = 5 \times 10^6$ J/m^3. The cubic magnetocrystalline anisotropy is described by W_{ani} $=\Sigma_{i=1}^{22}K_c t(M_{ix}^2 M_{iy}^2 + M_{iy}^2 M_{iz}^2 + M_{iz}^2 M_{ix}^2)$. Finally, for the interlayer coupling we used the phenomenological model for

bilinear (J_1) and biquadratic (J_2) exchange: W_{exc} $=-\Sigma_{i=1}^{21}[J_1(\vec{M}_i \cdot \vec{M}_{i+1}) + J_2(\vec{M}_i \cdot \vec{M}_{i+1})^2]$. To solve the Landau-Lifshitz equations at each new field value, the starting point was the spin configuration obtained at the previous field value, slightly randomly perturbed in order not to stabilize shallow local energy minima. The easy axis [Fig. 1(a)] and hard axis [Fig. 1(b)] hysteresis curves are consistently analyzed with the following constants: $K_c = 4.73(2) \times 10^4$ J/m^3, $J_1 = -0.74(1) \times 10^{-3}$ J/m^2, and $J_2 = -0.37(2) \times 10^{-4}$ J/m^2. The cubic magnetocrystalline anisotropy is close to the bulk value,[12] and the interlayer coupling constants are comparable to values obtained earlier.[13]

The calculations enable one to unravel the magnetization behavior near the nonsymmetric to symmetric transition when the magnetic field is applied in the hard-axis direction. The red lines in Figs. 1 and 2 were calculated with increasing field, starting from a simple antiferromagnetic configuration at zero field. The dashed blue lines in Fig. 2 were obtained on reducing the field from saturation. We plot the component of the normalized integrated moment parallel to the field [Fig. 2(a)] and transverse to the field [Fig. 2(b)]. The static susceptibility—i.e., the numerical derivative of the integrated parallel moment—is shown in Fig. 2(c). The energy density W is shown in Fig. 2(d).

In the case of increasing field (red curves), applying small fields, up to 40 mT, induces both a parallel and a transverse moment, characteristic of the field-induced nonsymmetric state. Contrary to what may be expected, however, the transition at 40 mT is not the nonsymmetric to symmetric transition. Indeed, the transverse moment above the critical field of 40 mT is reduced but definitely not zero. This behavior can be understood from the plots of the spin configurations at selected field values, presented on the right-hand side in Fig. 2. Close to the transition at 40 mT, the outer layer is excessively canted and about to overcome the crystalline anisotropy. Beyond the transition a discommensuration (or "stack-
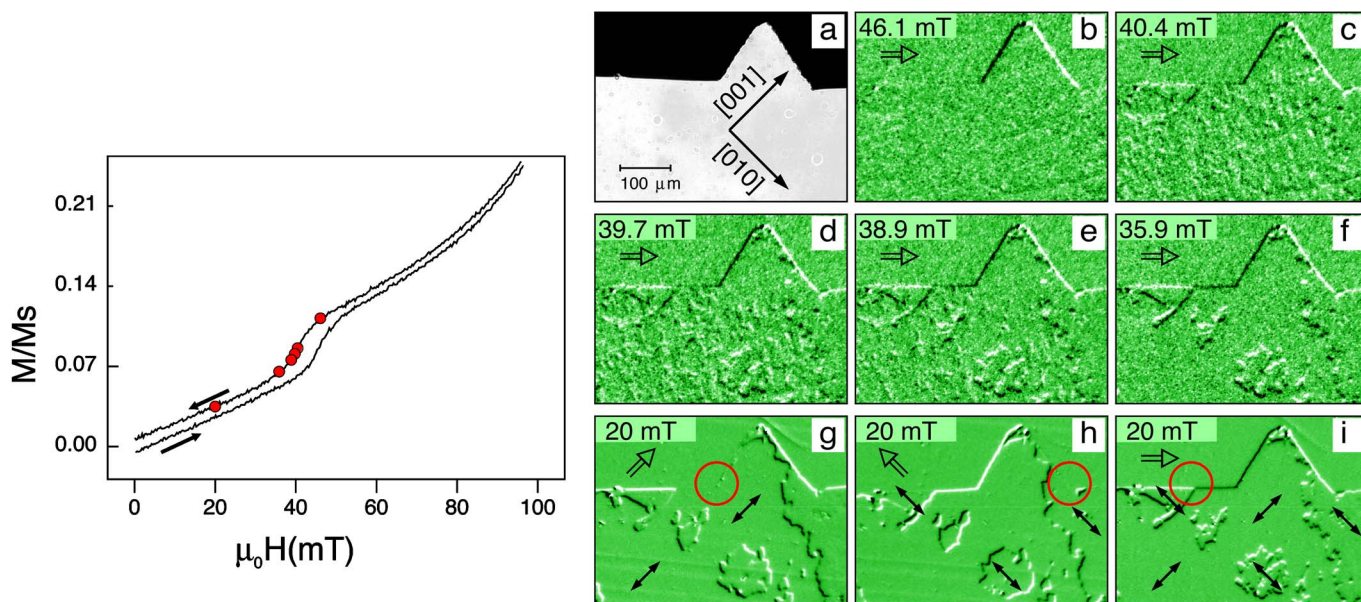
FIG. 3. (Color online) Left: detail of the hard-axis hysteresis curve for the Fe/Cr multilayer. The red dots indicate the points at which magneto-optic images are presented. Right: (a) conventional optical image of the sample, (b)–(f) magneto-optic indicator film images during demagnetization along the [011] hard axis, and (g)–(i) magneto-optic indicator film images with the field applied in various directions. The applied magnetic field and its direction are indicated in the upper left corner of each panel.

ing fault") is formed near the surface. The discommensuration penetrates into the superlattice with increasing field, until it reaches the center at 65 mT. The penetration of the discommensuration occurs in discrete steps, reflected as sharp peaks in the static susceptibility. Only at fields larger than 65 mT is the spin configuration macroscopically symmetric. The plots of the spin configurations clearly demonstrate the surface character of the transition.

If the field is adiabatically reduced from saturation, the calculations predict the transverse moment to be zero at all fields [dashed blue line in Fig. 2(b)]. In contrast with the situation of increasing fields, now the configuration is characterized by a nonvanishing parallel moment down to zero field [Fig. 2(a)]. These macroscopic properties are the manifestation of a symmetric spin configuration with a discommensuration that is trapped in the center of the superlattice, referred to as a twisted state. The spin configuration is illustrated on the right-hand side in Fig. 2.

These results are reminiscent of the surface spin-flop transition in uniaxial antiferromagnets, particularly in Fe/Cr(211) multilayers with uniaxial anisotropy. The surface spin-flop transition presented as red curves in Fig. 2 for the biaxial case and the magnetic field along the hard axis is very similar to the one predicted theoretically[1,2] and verified experimentally[3,6] for the uniaxial case and the magnetic field along the easy axis. Also, the theoretical prediction of a twisted state to exist down to remanence (blue line in Fig. 2) is in line with the uniaxial case.[4] However, in Fe/Cr(211) multilayers this twisted state was not found experimentally.[6] Therefore, it is worth further investigating the stability of the twisted state, also in the present case.

Theoretical input is obtained from the total energy of the spin configurations, presented in Fig. 2(d). Below 40 mT, the field-induced nonsymmetric state represented by the red curve is energetically most favorable. Above 40 mT, the energy difference between the red curve and blue curve is extremely small. For a perfectly layered multilayer system and at zero temperature, the Landau-Lifshitz calculations predict that the blue line is followed when reducing the field from saturation; i.e., the symmetric state above 40 mT evolves into the twisted state below 40 mT. In reality, however, small irregularities may shift the energy balance such that either the red curve or blue curve becomes more favorable above 40 mT. In addition, at fields smaller than 40 mT, thermal excitations may drive the transition from the metastable twisted state (blue curve) to the nonsymmetric state (red curve).

Thus, we need to verify experimentally whether the twisted state or nonsymmetric state is stabilized when reducing the field to low values. From the magnetization curves, it is, however, difficult to discriminate between both states. A closer look at the experimental hysteresis curve (Fig. 3) shows a feature around 40 mT, but the transition is not as steep as theoretically expected [compare to Fig. 2(a)]. Also, there is a very small remanent magnetization at zero field, but its magnitude is too small to be a convincing indication of the twisted state. Finally, as will be shown below, domain formation prevents one from using macroscopic transverse moment measurements to deduce the spin configuration. Instead, we used local stray field observations and polarized-neutron reflectivity measurements to gain additional information.

III. MAGNETO-OPTIC INDICATOR FILM IMAGING

The magneto-optic indicator film (MOIF) technique[14,15] is based on the Faraday effect: certain transparent media are able to rotate the plane of linear polarization of light in the

presence of magnetic fields parallel to the propagation direction of the light. An yttrium-iron garnet indicator film with in-plane anisotropy was placed on top of the sample. Stray fields emerging from the sample locally rotate the magnetization of the garnet out of plane. Tuning of the polarizer-analyzer pair, integrated in a light microscope, permits one to turn differences in the out-of-plane magnetization components into variations of the light intensity. In Fig. 3, we plot the ratio between two images taken with opposite polarization. An average is taken over 30 pairs of images and corrected for a slow background drift. White and black colors correspond to an increase and decrease of 2% with respect to the average ratio. The images visualize a region of the sample where it incidentally cleaved with a small triangular shaped extension whose edges are approximately along the [100] and [010] crystallographic directions of the multilayer [see Fig. 3(a)]. We verified that the behavior reported for this region is representative of the whole sample.

No contrast was observable from the multilayer in zero field, irrespective of the magnetic field history. This is consistent with the antiferromagnetic ordering of the Fe layers. As the spins of neighboring layers are oriented antiferromagnetically, the net moment of the multilayer at remanence is zero. Figure 3(b) was recorded at an external field of 46.1 mT applied along the [011] direction. Stray fields emerge wherever the divergence of the magnetization is nonzero—for example, where the induced net magnetic moment has a component perpendicular to the edge of the sample. In Fig. 3(b), the induced moment along the [011] direction gives rise to stray fields at the edges of the extrusion. Note that there are no stray fields along the [011] edges. This implies that the net moment perpendicular to the [011] direction vanishes: at this field the moments of the sublattices remain symmetrical with respect to the applied field.

The divergence of the net magnetization is also nonzero at the border between two antiferromagnetic domains for which the induced net magnetic moment is different. The patterns in Figs. 3(b)–3(f) visualize the process of domain formation during the in-plane [011] hard-axis demagnetization process. At a field of 40.4 mT [Fig. 3(c)] a grainy image is captured. Further decreasing the external magnetic field, the domains coalesce into larger domains [Figs. 3(d) and 3(e)]. The process of domain growth is completed at 35.9 mT [Fig. 3(f)]. The contrast fades at very small fields, but the domain structure is still present, even at zero field, since exactly the same domain structure reappears when small fields are applied.

In order to determine the orientation of the magnetization in the domains, an external magnetic field of 20 mT was applied in different directions [Figs. 3(g)–3(i)]. In Fig. 3(g), the field is along the [001] easy axis and thus parallel to the spins in domains with the magnetization along [001]. These domains are easily identified, as no torque is exerted on the spins and no net moment is induced. Consequently, these domains generate no stray fields on the sample edges (see the red circle). In a similar way, the domains with the magnetization along [010] were identified in Fig. 3(h). The deduced magnetization directions are indicated by the black arrows.

Figures 3(f) and 3(i), with the field along the [011] axis, show stray fields along the edge of the extrusion. But in addition, stray fields are now also observable along the edge

parallel to the [011] direction. Domains with the magnetization along the [001] direction generate black regions along the [011] edge, indicating that there is a field-induced transverse moment along the [01 −1] direction. Analogously, domains with the magnetization along the [010] direction generate white regions along the [011] edge, and thus they have a field-induced transverse moment along the [0 −11] direction. The fact that Fig. 3(f) reveals the presence of stray fields along the [011] edge is direct proof of the low-field spin configuration exhibiting a nonzero transverse component and thus being nonsymmetric. Note that the transverse component cannot be determined with a macroscopic magnetization measurement, since the field-induced transverse moment for neighboring domains is opposite.

In passing, we note that the calculated magnetization behavior presented in Fig. 2 may also explain the emergence of a domain structure when reducing the field below 46.1 mT and the increase of the domain size when further lowering the field. At $\mu_0 H = 40.4$ mT, the transverse magnetic moment is large [red curve in Fig. 2(b)]. Therefore, many small domains are stabilized to minimize the magnetostatic energy [Fig. 3(c)]. With further decreasing field, the transverse component in the magnetization decreases. Consequently, the magnetostatic energy decreases and domain growth may occur [Figs. 3(d) and 3(e)].

To summarize, the magneto-optic indicator film images provide a direct experimental proof of the presence of the nonsymmetric state at small external fields. This shows that, even in decreasing fields, the spin configuration assumes the energetically most favorable situation (red lines in Fig. 2).

IV. POLARIZED-NEUTRON REFLECTIVITY

Polarized-neutron reflectivity has proven particularly well suited to gain depth-selective information on the magnetic profile of Fe/Cr multilayered structures.[6,17,19] We performed polarized-neutron reflectivity measurements at the V6 beamline of the Hahn-Meitner Institut in Berlin. The incoming neutrons had a wavelength of $\lambda = 0.466$ nm and were polarized spin down by means of a supermirror. A spin flipper changed the spin of the neutrons to the opposite direction. Spin analysis of the reflected beam was achieved with a second supermirror, which transmits spin-down neutrons and reflects spin-up neutrons, in combination with an array of ^{3}He-gas-filled detector tubes. As a result, for each measurement, four intensities were recorded as a function of the angle of incidence θ or, equivalently, as a function of the neutron momentum transfer perpendicular to the surface $Q_z = 4\pi \sin \theta / \lambda$. The intensities are denoted R^{++}, R^{+-}, R^{-+}, and R^{--}, where the first and second superscripts indicate the neutron spin state before and after reflection from the sample, respectively.[18] The neutron spin can be either parallel (+) or antiparallel (−) to the applied field.

The interaction of the neutron with the material can be described by an effective optical potential $\Gamma = 4\pi N(b+p)$, with b the nuclear contribution to the scattering length, p the magnetic contribution to the scattering length, and N the number density. The densities for Fe and Cr are $N_{\text{Fe}} = 84.9$ nm^{-3} and $N_{\text{Cr}} = 83.3$ nm^{-3}, and the nuclear scattering
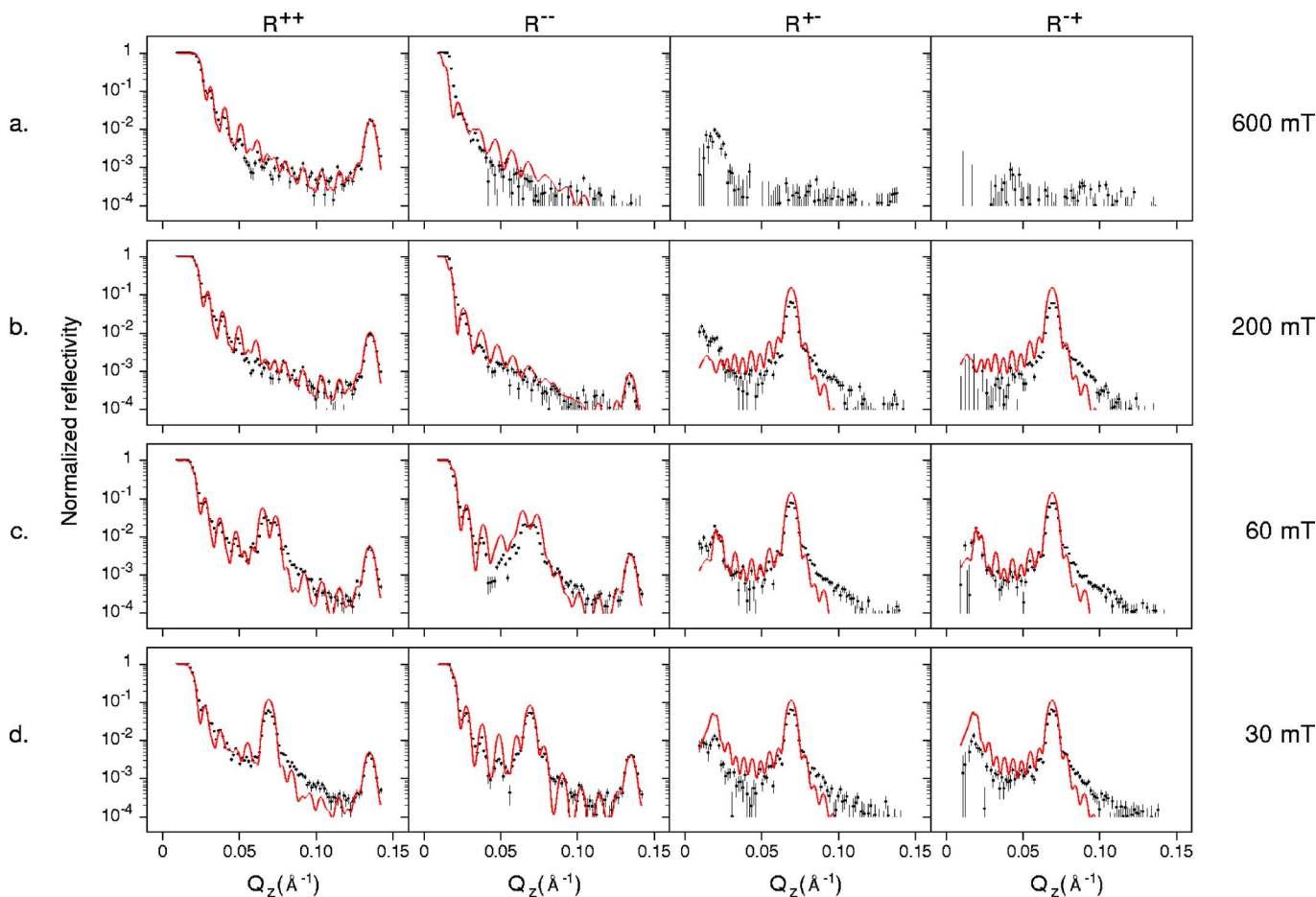
FIG. 4. (Color online) Polarized-neutron reflectivity spectra recorded at different magnetic fields indicated on the right. The solid lines are simulations as described in the text. The normalized reflectivity is plotted on a logarithmic scale and is limited to the value 10^{-4} for clarity. Therefore, the simulated spin-flip reflectivities at 600 mT, being very close to zero, do not appear in the graph.

lengths are $b_{Fe}=9.45$ fm and $b_{Cr}=3.635$ fm.[16] When the scattered neutrons do not change their spin state (R^{++} and R^{--}), the process is indicated as non-spin-flip scattering, and the magnetic scattering length p is proportional to the magnetization component along the neutron spin direction: e.g., $p = \pm 5.875$ fm when the magnetization in the Fe layers is parallel or antiparallel to the neutron spin. On the other hand, the spin-flip reflectivities (R^{+-} and R^{-+}) depend on the magnetization component perpendicular to the neutron spin. All together, the four reflectivity curves (R^{++}, R^{--}, R^{+-}, and R^{-+}) are a sensitive signature of both the longitudinal and transverse magnetization components as a function of the depth.

Reflectivity curves were recorded on the Fe/Cr multilayer with an external magnetic field applied along the in-plane hard axis. The experimental results obtained for different field values are shown in Fig. 4. The analysis of the data was carried out as follows. First, the polarized neutron reflectivity data taken in saturation (600 mT) were fitted assuming a uniform magnetic structure (all Fe spins aligned with the field). With the magnetic contrast suppressed the chemical structure is deduced. Next, the Landau-Lifschitz equation of motion was used to calculate the orientation of the spins in each Fe layer at the different field values (see Sec. II, increasing field). Finally, the resulting spin configuration was

used to calculate the polarized-neutron reflectivity in the kinematic approximation.[20] The results are shown as solid lines in Fig. 4. For a better understanding of the reflectivity data, we also plot the optical potential based on the calculated spin configuration (Fig. 5).

First, polarized-neutron reflectivity data were recorded while the sample was saturated in an external magnetic field of 600 mT [Fig. 4(a)]. The very small intensity in the spin-flip reflectivities (R^{+-} and R^{-+}) reflects the absence of a transverse moment, which is in agreement with the observation that the sample is magnetically saturated (Fig. 1). Apart from the total thickness oscillations, the R^{++} reflectivity exhibits an intensity maximum at $Q_z=0.135$ Å^{-1}, corresponding to diffraction from the chemical periodicity of the multilayer. The R^{--} reflectivity, on the other hand, does not show an intensity maximum in this region. This is understood by considering the optical potential for spin-up and spin-down neutrons as a function of depth from the surface, shown in Fig. 5. At 600 mT, the optical potential for spin-up neutrons (solid red lines) alternates between 0.016 35 nm^{-2} in the Fe layers and 0.003 810 nm^{-2} in the Cr layers. The pronounced contrast with a bilayer periodicity results in the strong Bragg reflection in the spin-up (R^{++}) scattering. The optical potential for spin-down neutrons (blue dotted lines)
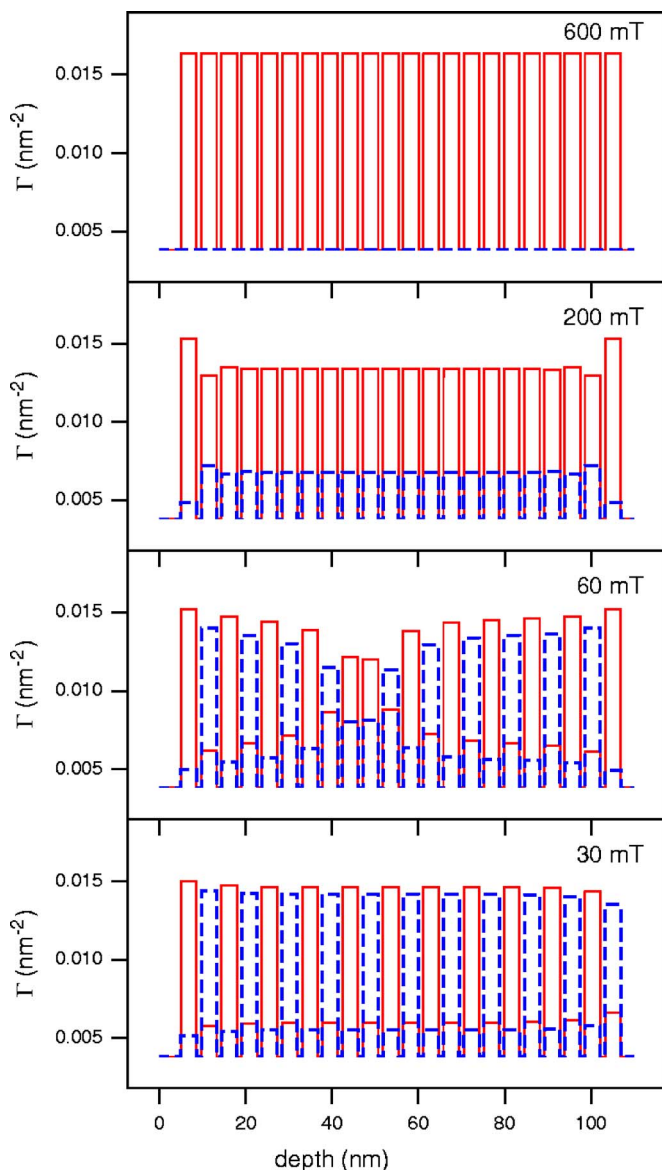
FIG. 5. (Color online) The optical potential as a function of the depth from the surface, based on the calculated spin configurations of Fig. 2. The solid red and dashed blue lines represent the optical potential for spin-up and spin-down neutrons, respectively.

in Fe is reduced to 0.003 814 nm^{-2} and thus nearly coincides with the one in Cr. The absence of a contrast explains the absence of a Bragg reflection for spin-down (R^{--}) scattering.

The reflectivity curves that were obtained in an external magnetic field of 200 mT are shown in Fig. 4(b). As a main difference with the spectra at 600 mT, one immediately observes the strong intensity featuring a peak at $Q_z=0.07$ Å^{-1} in the spin-flip reflectivities (R^{+-} and R^{-+}). Indeed, upon reducing the external magnetic field to 200 mT, the Fe magnetic moments find two alternating easy-axis directions as energetically favorable (see the spin configuration plotted in Fig. 2, 200 mT). This results in a two-bilayer periodicity for the transverse component of the magnetization, which in turn gives rise to a half-order Bragg peak in the spin-flip reflectivities (R^{+-} and R^{-+}). Furthermore, one notes at $Q_z=0.135$ Å^{-1} that the R^{++} intensity has decreased and the R^{--}

intensity has increased, reflecting a reduction of the net parallel moment at smaller applied fields.

Particularly interesting spectra were obtained in an applied field of 60 mT [Fig. 4(c)]. In this case, at $Q_z=0.07$ Å^{-1}, the half-order Bragg peaks in the spin-flip reflectivities are accompanied with split half-order peaks in the non-spin-flip reflectivities. The half-order Bragg peaks in R^{+-} and R^{-+} indicate a regularly alternating transverse component of the magnetization with a two-bilayer periodicity. The half-order Bragg peaks in R^{++} and R^{--} indicate that the longitudinal component of the magnetization also has a two-bilayer periodicity. This is illustrated in the plot of the optical potential (Fig. 5, 60 mT). Thus, at 60 mT the magnetization of neighboring Fe layers has an antiferromagnetic component along the field direction. The splitting of the half-order Bragg peak arises from a discommensuration in the antiferromagnetic ordering, as is seen from the optical potential at a depth of 46.2 nm. A similar feature was observed, also via polarized-neutron reflectivity measurements, during the surface spin-flop transition in antiferromagnetically coupled Fe/Cr(211) superlattices with uniaxial anisotropy[6] and in the bulk spin-flop phase in an Fe/Cr(100) superlattice.[19]

The spectra recorded at 30 mT [Fig. 4(d)] show a strong half-order Bragg peak at $Q_z=0.07$ Å^{-1} with comparable intensity in all four reflectivities. Since the easy axis is at 45° with respect to the applied field direction, one obtains nearly identical moment projections in both directions, such that both the spin-flip and non-spin-flip reflectivities show a half-order Bragg peak of equal intensity. The fact that the half-order Bragg peaks in R^{++} and R^{--} are not split is direct proof of the spin configuration not containing a discommensuration trapped in the center. Moreover, the first-order Bragg peak at $Q_z=0.135$ Å^{-1} has practically the same intensity in R^{++} and R^{--}. This proves that the net moment along the field direction has almost vanished. These two observations confirm that the energetically most favorable spin configuration (red lines in Fig. 2) is stabilized at low fields.

In the analysis of the polarized-neutron reflectivity data the thickness and roughness were varied to fit the spectra at 600 mT, but were fixed parameters for the simulations at other fields. Moreover, the magnetic profile was deduced from the Landau-Lifshitz calculations. Therefore, no free parameters were used for the simulations at 200, 60, and 30 mT, and yet, we observe only a small misfit between the simulations and experimental data. The remaining misfit, particularly around $Q_z=0.07$ Å^{-1} in the spin-flip scattering, may be attributed to the fact that a homogeneous in-plane magnetization was assumed, although the magneto-optic images have shown the presence of domains that differ in the transverse component. As a result, whereas the parallel moment is coherent and thus the non-spin-flip scattering is presumably specular, the transverse component is inhomogeneous and may lead to off-specular scattering and a reduced specular scattering.

We conclude that the simulations reproduce the important features in the experimental data in Fig. 4. This supports the validity of the spin configurations that were obtained from the Landau-Lifschitz calculations. The data could only be reproduced with the nonsymmetric configurations of the magnetization in Fig. 2. Therefore, the neutron data confirm

that the energetically most favorable spin state is assumed, in both increasing and decreasing field sweeps.

V. CONCLUSIONS

We studied the spin configuration in an antiferromagnetically coupled Fe/Cr(100) superlattice with cubic crystalline anisotropy when the field is applied along the in-plane hard magnetization axis. Using micromagnetic calculations, we show that increasing fields give rise to a surface spin-flop transition. The surface transition found here bears a remarkable resemblance to the surface spin-flop for antiferromagnets with uniaxial anisotropy. The spin configuration was further investigated experimentally.

We show that magneto-optic indicator film imaging is a suitable technique to visualize the domain behavior in antiferromagnetically coupled multilayers. Images taken in decreasing fields show that the low-field spin configuration is *not* the twisted state with a discommensuration trapped in the center. Instead, they reveal a net transverse magnetization component characteristic of the field-induced nonsymmetric state. We pointed out the importance of the magnetostatic energy connected to the transverse moment in the domain formation.

Polarized-neutron reflectivity measurements permitted us to probe the magnetic profile depth selectively. A ferromagnetic ordering is probed at high magnetic fields. At intermediate fields (60 mT), a discommensuration is formed near the middle of the multilayer stack. At 30 mT, the absence of a splitting of the half-order Bragg peak shows that the discommensuration has disappeared and that the spins have stabilized into the nonsymmetric state. If the calculated nonsymmetric spin configuration from the micromagnetic calculations is adopted, then the simulations compare favorably with the experimental data.

To summarize, surface effects play an important role in the hard-axis magnetization behavior of antiferromagnetic materials with cubic anisotropy. Micromagnetic calculations faithfully reproduce the magnetization behavior of the sample in the easy- and hard-axis directions. The calculations are substantiated with observations from magneto-optic indicator film imaging and from polarized-neutron reflectivity measurements. The theoretical prediction of a twisted state in decreasing fields is not observed experimentally, which is attributed to small layer irregularities or thermal excitations.

*Electronic address: Johan.Meersschaut@fys.kuleuven.be

[1] D. L. Mills and W. M. Saslow, Phys. Rev. **171**, 488 (1968).

[2] F. Keffer and H. Chow, Phys. Rev. Lett. **31**, 1061 (1973).

[3] R. W. Wang, D. L. Mills, E. E. Fullerton, J. E. Mattson, and S. D. Bader, Phys. Rev. Lett. **72**, 920 (1994).

[4] N. Papanicolaou, J. Phys.: Condens. Matter **10**, L131 (1998).

[5] C. Micheletti, R. B. Griffiths, and J. M. Yeomans, Phys. Rev. B **59**, 6239 (1999).

[6] S. G. E. teVelthuis, J. S. Jiang, S. D. Bader, and G. P. Felcher, Phys. Rev. Lett. **89**, 127203 (2002).

[7] T. C. Schulthess and W. H. Butler, Phys. Rev. Lett. **81**, 4516 (1998).

[8] A. Hoffmann, Phys. Rev. Lett. **93**, 097203 (2004).

[9] P. Grünberg, R. Schreiber, Y. Pang, M. B. Brodsky, and H. Sowers, Phys. Rev. Lett. **57**, 2442 (1986).

[10] S. S. P. Parkin, N. More, and K. P. Roche, Phys. Rev. Lett. **64**, 2304 (1990).

[11] B. Dieny, J. P. Gavigan, and J. P. Rebouillat, J. Phys.: Condens. Matter **2**, 159 (1990).

[12] R. O'Handley, *Modern Magnetic Materials: Principles and Applications* (John Wiley & Sons, New York, 2000).

[13] M. Grimsditch, S. Kumar, and E. E. Fullerton, Phys. Rev. B **54**, 3385 (1996).

[14] V. K. Vlasko-Vlasov, G. W. Crabtree, U. Welp, and V. I. Nikitenko, in *Physics and Materials Science of Vortex States, Flux Pinning and Dynamics*, edited by R. Kossowsky *et al.*, Vol. 356 of NATO Advanced Study Institute, Ser. E (Kluwer Academic, Dordrecht, 1999), p. 205.

[15] L. H. Bennett, R. D. McMichael, L. J. Swartzendruber, S. Hua, D. S. Lashmore, A. J. Shapiro, V. S. Gornakov, L. M. Dedukh, and V. I. Nikitenko, Appl. Phys. Lett. **66**, 888 (1995).

[16] V. F. Sears, Neutron News **3**(3), 29 (1992), http://www.ncnr.nist.gov/resources/n-lengths/.

[17] A. Schreyer, J. F. Anker, T. Zeidler, H. Zabel, C. F. Majkrzak, M. Schäfer, and P. Grünberg, Europhys. Lett. **32**, 595 (1995).

[18] J. F. Anker and G. P. Felcher, J. Magn. Magn. Mater. **200**, 741 (1999).

[19] V. Lauter-Pasyuk, H. J. Lauter, B. P. Toperverg, L. Romashev, and V. Ustinov, Phys. Rev. Lett. **89**, 167203 (2002).

[20] F. Ott, T.-D. Doan, P. Humbert, and C. Fermon, Computer code SIMULREFLEC, Laboratoire Léon Brillouin CEA/CNRS, 2001, http://www-llb.cea.fr / prism / programs / simulreflec / simulreflec.html